

Long term sedimentation of an elliptic disc subject to an electrostatic field using smoothed particle hydrodynamics method

N. Tofighi^{a,*}, J. J. Feng^{b,c}, M. Yildiz^{d,e,f}, A. Suleman^a

^aDepartment of Mechanical Engineering, University of Victoria, Victoria, BC V8P 5C2, Canada

^bDepartment of Mathematics, University of British Columbia, Vancouver, BC V6T 1Z2, Canada

^cDepartment of Chemical and Biological Engineering, University of British Columbia, Vancouver, BC V6T 1Z3, Canada

^dFaculty of Engineering and Natural Sciences (FENS), Sabanci University, Tuzla, 34956, Istanbul, Turkey

^eIntegrated Manufacturing Technologies Research and Application Center, Sabanci University, Tuzla, 34956, Istanbul, Turkey

^fComposite Technologies Center of Excellence, Sabanci University-Kordsa, Istanbul Technology Development Zone, Pendik, 34906, Istanbul, Turkey

Abstract

A two dimensional incompressible smoothed particle hydrodynamics scheme for long term sedimentation of rising or falling particulates (bubbles, drops or rigid particles) in Newtonian fluids is presented and validated by simulating the sedimentation of a single elliptic disc. The proposed method is then used to simulate the sedimentation of an elliptic disc subject to an external electric field parallel to the gravitational field. A range of electric field intensities, permittivity ratios, blockage ratios and density ratios are covered in this study. The results show that for given blockage and density ratios, the final sedimentation orientation of the ellipse is dependent on a combination of permittivity ratio and electric field intensity, ranging from horizontal to vertical. Compared to non-electrified sedimentation, an increase in electric field intensity and permittivity ratio lead to vertical sedimentation. As the channels grow wider, the presence of electric field leads to faster ellipse descent, regardless of its initial orientation.

*Corresponding author

Email addresses: nima@sabanciuniv.edu (N. Tofighi), james.feng@ubc.ca (J. J. Feng), meyildiz@sabanciuniv.edu (M. Yildiz), suleman@uvic.ca (A. Suleman)

Keywords: Fluid-Particle Interaction, Sedimentation, Electric Field, Smoothed Particle Hydrodynamics, Shifting Boundary

1. Introduction

Sedimentation of small particles in a background fluid is a prevalent phenomenon in many natural and industrial applications such as meteorology, sedimentology, biomechanics and chemical engineering ([Field et al., 1997](#)). A few examples include the motion of atmospheric aerosols, hailstone growth, falling of winged seeds, river erosion, slurry transport and sedimentation of colloidal particles. The paths traversed by the particles in these buoyancy driven flows are highly dependent on particle shapes, proximity of bounding walls and density ratio, ranging from a straight line to chaotic. A detailed review of the path and wake of falling particles is given by [Ern et al. \(2012\)](#).

Most of the particles found naturally are of non-spherical shapes. Among non-spherical geometries, spheroids and ellipsoids in three dimensions as well as ellipses in two dimensions have been the subject of many studies. [Cox \(1965\)](#) showed that a prolate spheroid sedimenting in infinite fluid will align its major axis perpendicular to the falling direction. [Feng et al. \(1994\)](#) simulated the sedimentation of an ellipse between parallel walls and observed a gradual change in behavior with increasing Reynolds number. In a later work, [Feng and Joseph \(1995\)](#) simulated the interactions of two sedimenting ellipses in Stokes regime. [Aidun et al. \(1998\)](#) further investigated the interactions of two ellipses at larger Reynolds number. [Swaminathan et al. \(2006\)](#) simulated the sedimentation of a prolate spheroid in a sufficiently large tube and observed that for finite Reynolds numbers, the spheroid settles with its major axis perpendicular to the direction of gravity. [Xia et al. \(2009\)](#) covered a wide range of blockage ratios for sedimenting ellipses. They report that the ellipse adopts different patterns of sedimentation for low blockage ratios and the final mode of sedimentation depends on the initial conditions. In a similar work, [Yang et al. \(2015\)](#) studied the sedimentation of prolate spheroids in narrow tubes and made similar

observations.

Once particle and sedimenting environment properties are fixed, there is no control over the trajectory of sedimenting particles. It is possible to modify the particle behavior indirectly by introducing shear or pressure drop in fluid medium. Alternatively, use of an external magnetic or electric field affects orientation and translational motion of the particles directly. Electric fields are widely used to modify the behavior of particles in controlling clustering in sedimenting colloids (Newman and Yethiraj, 2015; Sullivan et al., 2003; Chang and Keh, 2013; Lee et al., 2000), electrorheological fluids (Parthasarathy and Klingenberg, 1996; Bonnecaze and Brady, 1992) and assembly of colloidal particles and biological cells (House et al., 2012; Velev et al., 2009). Despite the aforementioned applications, the sedimentation of an elliptic particle in an external electric field has not been studied in detail.

In this study, we consider the sedimentation of a single non-conductive ellipse subject to parallel electric and gravitational fields. As such, we disregard particle-particle interactions due to flow and electric fields observed in denser suspensions. To simplify our analysis, we assume thin electric double layer. This means at its smallest, the ellipse must be micron sized (Ai and Qian, 2010). Furthermore, we assume zero surface charge, thus neglecting translational electrophoretic motion of the particle parallel to the electric field direction. As both electrophoresis and buoyancy act in parallel, this assumption does not lead to a substantial change in the qualitative sedimentation behavior. When placed in an external electric field, a non-conductive elliptic particle will rotate to align its major axis with the direction of electric field (House et al., 2012). This in turn leads to different sedimentation behavior when compared to an ellipse descending in non-electrified medium.

First developed by Lucy (1977) and Gingold and Monaghan (1977), smoothed particle hydrodynamics (SPH) is a Lagrangian meshless spatial discretization method. SPH has been used extensively to study particle dynamics in the absence of an external electric field. Zhang et al. (2018) have simulated the interaction of multiple discs during sedimentation and later expanded their in-

vestigations to thermal effects (Zhang et al., 2019). SPH coupled with discrete element method has also been used to simulate the interaction of multiple three dimensional particles (Robinson et al., 2014; He et al., 2018; Joubert et al., 2020) under different configurations. In this work, a two dimensional incompressible SPH (ISPH) method is used to solve the governing equations of fluid flow and electric fields. The numerical method has been extensively tested in our previous works for the motion of particles with and without electric fields (Tofighi et al., 2015). However, to our knowledge, no boundary conditions currently available in SPH support effortless simulation of infinitely long sedimentation while such studies are common using other methods (Xia et al., 2009; Swaminathan et al., 2006). To alleviate this shortcoming, a boundary condition supporting infinite falling or rising motion is developed here. The method relies on shifting the computational domain vertically to keep the features of interest close to the central region. SPH particles are added or discarded near domain boundaries as bounding walls shift. For a sufficiently long channel, the boundary effects are negligible and unlimited rising or falling motion of bubbles, drops or rigid particles may be simulated.

The proposed method for ISPH simulation of unlimited falling or rising motion is used to simulate the sedimentation of an elliptic disc. The results are compared to literature data and good agreement is observed. The method is then used to simulate the motion of an elliptic disc sedimenting in an external electric field. Our results show that applying the electric field increases the sedimentation velocity in wider channels. Further increase of the field intensity will only result in an increase in descent velocity until the ellipse aligns its major axis with the field direction. The rest of this writing is structured as follows: we describe the governing scales and equations as well as the numerical method in sections 2-4. Implementation of the boundary condition and its validation are discussed in section 5. The sedimentation of elliptic disc in an external electric field is covered in section 6 and concluding remarks are drawn in section 7. From this point forward, the term “particle” will refer to the SPH particles used to discretize the computational domain.

2. Geometry and scales

A schematic of the case considered in this study is shown in figure 1. The ellipse, with major axis a and minor axis b , is placed at the midpoint between vertical walls at an angle θ with the horizontal axis. The channel is W wide and vertically “unlimited”. As a result, channel height is not included as a parameter here and the boundary treatment will be further clarified in section 5. All side walls comply with no slip and no penetration conditions. A constant potential difference is applied to horizontal walls while vertical walls are electrically insulated. The external electric and gravitational fields are aligned with the vertical axis along the channel.

A typical set of characteristic values for an incompressible, isothermal and electrically insulating Newtonian fluid subject to an external electric field may be chosen as

$$\begin{aligned} x_c &= a, & g_c &= g_\infty & \rho_c &= \rho_f, & \mu_c &= \mu_f, & E_c &= E_\infty, & \varepsilon_c &= \varepsilon_v \varepsilon_f, \\ u_c &= \sqrt{g_c x_c}, & p_c &= \rho_c u_c^2, & t_c &= x_c/u_c \end{aligned} \quad (1)$$

where ρ , μ , t , u , p , g , E and ε denote density, viscosity, time, velocity, pressure, gravity, electric field intensity and electric permittivity, respectively. Subscript \square_f marks fluid values while subscript \square_c is used to denote characteristic values. Additionally, g_∞ , E_∞ , ε_v and ε_f are gravitational field intensity, undisturbed electric field intensity produced by the imposed potential difference between horizontal walls, permittivity of vacuum and relative permittivity of the fluid.

Based on the characteristic values given in equation (1), we define Reynolds and Electrogravitational numbers as

$$\text{Re}_p = \frac{\rho_f \sqrt{g_\infty a^3}}{\mu_f}, \quad \text{Eg}_p = \frac{\rho_f g_\infty a}{\varepsilon_v \varepsilon_f E_\infty^2}, \quad (2)$$

along with the following set of dimensionless numbers to describe the system

$$\mathcal{D} = \rho_s/\rho_f, \quad \mathcal{P} = \varepsilon_s/\varepsilon_f, \quad \mathcal{A} = a/b, \quad \mathcal{B} = W/a, \quad (3)$$

where \mathcal{D} is density ratio, \mathcal{P} is permittivity ratio, \mathcal{A} is aspect ratio, \mathcal{B} is blockage ratio and \square_s is used to denote solid values. Following prior works (Xia et al.,

2009; Suzuki and Inamuro, 2011; Khorasanizade and Sousa, 2016), Reynolds number and aspect ratio are set to $\mathcal{A} = 2$ and $\text{Re}_p = 100$ for all simulations in this study. Unless otherwise mentioned, all variables after this point are given in dimensionless form based on characteristic scales of equation (1). Additionally, we will refer to the position and velocity of the center of the ellipse as ellipse position and ellipse velocity for brevity. To compare with other studies, an alternative form of Reynolds number based on average velocity is also defined as

$$\text{Re}_t = \frac{\rho_f u_v a}{\mu_f}, \quad (4)$$

where u_v is a vertical velocity. For cases with a terminal velocity, u_v is taken equal to the ellipse descent velocity. When the ellipse descends in an oscillatory trajectory, the average ellipse descent velocity is used for u_v .

3. Governing equations

Assuming a thin electric double layer and neutral computational domain, the electric potential ϕ of non-conductive media may be calculated through

$$\nabla \cdot (\varepsilon \nabla \phi) = 0, \quad (5)$$

while the electric field is computed as the gradient of the electric potential, $\mathbf{E} = -\nabla \phi$ (Ai and Qian, 2010; Saville, 1997). The dimensionless form of the governing equations of the flow may be written as

$$\nabla \cdot \mathbf{u} = 0, \quad (6)$$

$$\rho \left(\frac{\partial \mathbf{u}}{\partial t} + \mathbf{u} \cdot \nabla \mathbf{u} \right) = -\nabla p + \frac{1}{\text{Re}_p} \nabla \cdot \boldsymbol{\tau} + \frac{1}{\text{Eg}_p} \mathbf{f}_{(e)} + \mathbf{f}_{(b)}, \quad (7)$$

$$\boldsymbol{\tau} = \mu [\nabla \mathbf{u} + (\nabla \mathbf{u})^\dagger], \quad (8)$$

$$\mathbf{f}_{(b)} = (\rho - 1) \mathbf{g}, \quad (9)$$

where vectors and tensors are shown in bold and superscript \square^\dagger denotes the transpose operation. Here, $\boldsymbol{\tau}$ is Newtonian stress tensor and $\mathbf{f}_{(b)}$ represents the

buoyancy force. The electric force vector $\mathbf{f}_{(e)}$ is calculated through divergence of Maxwell stress tensor (Saville, 1997),

$$\mathbf{f}_{(e)} = -\frac{1}{2}\mathbf{E} \cdot \mathbf{E} \nabla \varepsilon. \quad (10)$$

Separate color functions \hat{c}^α are used to identify each of the phases, where \square^α may denote fluid \square^f or solid \square^s phases. These functions assume unit value in phase α and zero in all other phases. Rigidity constraints are applied to ensure rigid behavior in the ellipse and its viscosity is set to one hundred times the fluid viscosity (Tofighi et al., 2015).

4. Numerical method

In SPH, the term particle is used to refer to the spatial elements discretizing the computational domain. The particle of interest i interacts with its neighboring particles j through an interpolation kernel w_{ij} (Monaghan, 2012). The kernel is a function of smoothing length h and r_{ij} , the magnitude of distance vector $\mathbf{r}_{ij} = \mathbf{r}_i - \mathbf{r}_j$. Here, we set $h = 1.6\delta_p$ where δ_p is the shortest distance between fluid particles in the initial arrangement.

The phase properties are interpolated using weighted harmonic mean,

$$\frac{1}{\chi_i} = \frac{c_i^f}{\chi_f} + \frac{c_i^s}{\chi_s}, \quad c_i^\alpha = \frac{1}{\psi_i} \sum_{j=1}^{J_n} \hat{c}_j^\alpha w_{ij}, \quad \psi_i = \sum_{j=1}^{J_n} w_{ij} \quad (11)$$

where χ may denote viscosity or permittivity, J_n is the number of neighboring particles and ψ_{ij} is the number density. The smoothed color function c^α produces a smoother transition and is calculated using the cubic spline kernel (Morris, 1996).

For the ellipse, center-of-mass velocity \mathbf{u}_s and angular velocity ω_s are computed by cycling over all particles J_d through

$$\mathbf{u}_s = \frac{1}{M_s} \sum_{j=1}^{J_d} \frac{\hat{c}_j^s \mathbf{u}_j}{\psi_j}, \quad \omega_s = \frac{1}{I_s} \sum_{j=1}^{J_d} \frac{\hat{c}_j^s \mathbf{u}_j \times \mathbf{r}_{js}}{\psi_j}. \quad (12)$$

which are then used to derive individual velocities of each particle as

$$\mathbf{u}_i = \hat{c}_i^f \mathbf{u}_i + \hat{c}_i^s [\mathbf{u}_s + \omega_s \times (\mathbf{r}_i - \mathbf{r}_s)]. \quad (13)$$

Here, M_s is the overall volume of particles belonging to the ellipse and I_s is the ellipse's moment of inertia about its center of mass $\mathbf{r}_s = \sum_{j=1}^{J_d} \hat{c}_j^s \mathbf{r}_j$ ([Tofighi et al., 2015](#)).

A predictor-corrector scheme is used to advance the governing equations in time where the timestep is calculated according to Courant-Friedrichs-Lowy condition ([Shao and Lo, 2003](#)),

$$\Delta t = \eta \min_{1 \leq j \leq J_d} \left(\frac{h}{u_j}, \frac{1}{\text{Re}_p} \frac{h^2 \rho_j}{2 \mu_j} \right), \quad (14)$$

where $\eta = 0.25$ ([Zainali et al., 2013](#)).

At n th timestep of the predictor step ($\square^{(n)}$), the artificial particle displacement (APD) vector $\delta \mathbf{r}_i^{(n)}$ is calculated according to the method used by [Tofighi et al. \(2015\)](#). The particles are then transferred to an intermediate position marked by superscript \square^+ via

$$\mathbf{r}_i^+ = \mathbf{r}_i^{(n)} + \mathbf{u}_i^{(n)} \Delta t + \hat{c}_i^0 \delta \mathbf{r}_i^{(n)}. \quad (15)$$

Number density and transport properties are updated through equation (11) while electric potential is calculated by solving equation (5). After calculating the electric forces through equation (10), intermediate velocities are computed through

$$\mathbf{u}_i^+ = \mathbf{u}_i^{(n)} + \frac{\Delta t}{\rho_i^+} \left[\frac{1}{\text{Re}_p} \boldsymbol{\nabla} \cdot \boldsymbol{\tau}_i + \frac{1}{\text{Eg}_p} \mathbf{f}_{(e)i} \right]^+. \quad (16)$$

In the corrector step, Poisson equation subject to zero gradient boundary condition,

$$\boldsymbol{\nabla} \cdot \left(\frac{1}{\rho^+} \boldsymbol{\nabla} p^{(n+1)} \right) = \frac{\boldsymbol{\nabla} \cdot \mathbf{u}^+}{\Delta t}, \quad (17)$$

is solved to compute the pressure at timestep $n + 1$. The pressure is then used to restore incompressibility to the velocity field through

$$\mathbf{u}_i^{(n+1)} = \mathbf{u}_i^+ - \frac{1}{\rho_i^+} \boldsymbol{\nabla} p_i^{(n+1)} \Delta t. \quad (18)$$

After imposing rigidity constraints through equations (12) and (13), the particles are moved to their final positions using

$$\mathbf{r}_i^{(n+1)} = \mathbf{r}_i^{(n)} + \frac{1}{2} \left(\mathbf{u}_i^{(n)} + \mathbf{u}_i^{(n+1)} \right) \Delta t + \hat{c}_i^f \delta \mathbf{r}_i^{(n)}. \quad (19)$$

The first derivative and Laplace operator of vector and scalar functions are approximated through following expressions

$$\frac{\partial f_i^m}{\partial x_i^k} a_i^{kl} = \sum_{j=1}^{J_n} \frac{1}{\psi_j} (f_j^m - f_i^m) \frac{\partial w_{ij}}{\partial x_i^l}, \quad (20)$$

$$\frac{\partial}{\partial x_i^k} \left(\varphi_i \frac{\partial f_i^m}{\partial x_i^k} \right) a_i^{ml} = 8 \sum_{j=1}^{J_n} \frac{\varphi_{ij}}{\psi_j} (f_i^m - f_j^m) \frac{r_{ij}^m}{r_{ij}^2} \frac{\partial W_{ij}}{\partial x_i^l}, \quad (21)$$

$$\frac{\partial}{\partial x_i^k} \left(\varphi_i \frac{\partial f_i}{\partial x_i^k} \right) (2 + a_i^{kk}) = 8 \sum_{j=1}^{J_n} \frac{\varphi_{ij}}{\psi_j} (f_i - f_j) \frac{r_{ij}^k}{r_{ij}^2} \frac{\partial w_{ij}}{\partial x_i^k}. \quad (22)$$

$$\varphi_{ij} = \frac{2\varphi_i\varphi_j}{\varphi_i + \varphi_j}, \quad a_i^{kl} = \sum_{j=1}^{J_n} \frac{r_{ij}^k}{\psi_j} \frac{\partial w_{ij}}{\partial x_i^l} \quad (23)$$

Here, a quintic spline kernel ([Monaghan and Kocharyan, 1995](#)) is employed to calculate the derivatives and a_i^{kl} is used to correct discrete kernel behavior ([Zainali et al., 2013](#)). Where appropriate, φ may denote density-inversed, viscosity or permittivity. The above method has been successfully used by [Tofighi et al. \(2019\)](#) to simulate the dielectrophoretic interaction of multiple circular discs in uniform electric fields.

5. Boundary conditions

There are two common approaches to implementing wall boundary conditions, slip or no-slip, in SPH. The first method is by introducing additional terms in governing equations to reproduce the desired behavior near the boundaries. Following this approach, [Monaghan and Kajtar \(2009\)](#) propose a repulsive force applied to particles approaching the boundaries. Another example is the semi-analytical method by [Ferrand et al. \(2013\)](#) where renormalization factors are computed to impose the boundary conditions. The second approach of implementing wall boundary conditions is by employing additional layers of particles. These auxiliary particles are placed outside the computational domain and complete the support domain of the fluid particles near the boundaries. [Morris et al. \(1997\)](#) proposed one such method where the auxiliary particle positions were

constant during the simulation and their velocities were interpolated from fluid particles while their densities were evolved. In another method developed by [Adami et al. \(2012\)](#), all properties of the static auxiliary particles were interpolated from fluid particles. [Yildiz et al. \(2009\)](#) developed multiple boundary tangent (MBT) method which uses dynamically positioned auxiliary particles to allow arbitrary boundary geometries.

Despite the large variety of wall boundary implementations in SPH, relatively few methods are developed for flow-through boundaries. While periodic boundary conditions are fairly simple to implement, the inflow and outflow boundary conditions require special treatments. [Lastiwka et al. \(2009\)](#) proposed an inflow boundary condition where auxiliary particles were arranged in layers behind the inlet and entered the computational domain as fluid particles. Layers of fluid particles exiting the domain were kept as auxiliary particles until they no longer affected the computational domain. The method of characteristics was used to compute the properties of the auxiliary particles. [Federico et al. \(2012\)](#) and [Hosseini and Feng \(2011\)](#) used a similar approach, however, they specified the properties of the auxiliary particles directly. [Hirschler et al. \(2016\)](#) used an alternative approach where inflow and outflow boundaries were simulated as moving walls.

The most straightforward way of simulating long term sedimentation of a solid object is to use a sufficiently long channel. However, this method imposes significant computational overhead as the region of interest around the solid body constitutes a very small portion of the entire computational domain. To circumvent this problem, one may use a smaller computational domain and move the region of interest with the falling body. Two different approaches may be taken to implement this idea. The first approach is to move the entire domain by the mean velocity u_m of the sedimenting body. In this case, vertical walls move at u_m and flow-through boundary conditions have to be applied to horizontal surfaces (figure 1). Periodic boundary conditions are not suitable for horizontal surfaces as the sedimenting body will face its own wake at later stages of simulation. As such, inflow and outflow boundary conditions are required. A problem

with this approach is that u_m is not known *a priori* and use of variable u_m requires modifications in governing equations (6-9), complicating the solution procedure and implementation of inflow and outflow boundaries. Alternatively, one may compensate for the vertical distance traveled by the sedimenting body by shifting the entire computational domain in the reverse direction. In this case, a solid body placed sufficiently far from the horizontal boundaries acts as if sedimenting in an infinitely long channel. Similar to the first approach, the periodic boundary condition is not applicable to horizontal walls. However, to our knowledge, there are no other suitable boundary conditions available in SPH literature.

In this study, we use a simplified form of MBT method to impose the no-slip boundary condition on vertical walls. We use the second approach of shifting the entire domain to simulate infinite sedimentation. For this purpose, a “shifting” boundary condition is developed and tested here. This boundary condition is also suitable for the simulation of falling droplets as well as rising solid bodies and bubbles.

5.1. Definition of the shifting boundary

Figure 2 shows a schematic of the shifting boundary condition for a descending feature. The particles near horizontal boundaries are shown with black outlines while the auxiliary particles are shown with gray outlines. Internal particles are shown as black squares. Incoming particles are shown with green fill while outgoing particles are marked with red fill. The feature of interest, shown as a large circle, is placed at an appropriate distance away from the horizontal walls. In this study, we place the ellipse at the midpoint between horizontal walls.

When released from its initial position, the ellipse is allowed to travel up to one particle spacing δ_p toward the bottom wall. During this time, the MBT method is used to apply the no-slip boundary condition on horizontal walls. Figure 2-a shows a configuration where the ellipse’s center of mass has moved beyond one particle spacing from its initial position. At this point, the position

of all particles within the computational domain are shifted up by δ_p to bring the ellipse close to the midpoint between horizontal walls. All other properties of the particles remain unchanged during this operation. The shifted configuration is shown in figure 2-b. Any particle transferred out of the computational domain and the particles residing closer than $\delta_p/2$ to the upper wall are discarded. These particles are shown as red filled squares in figure 2. To fill the gap left near the bottom wall, one row of auxiliary particles adjacent to the boundary are moved inside the computational domain and made into regular particles. These particles are shown in green before (figure 2-a) and after (figure 2-b) the operation.

To remove the wake effects near the upper boundary and avoid possible disturbances near the lower boundary, a hyperbolic tangent damping function is used to nullify particle velocity near the boundaries. Here we used a damping function with an effective range of $10\delta_p$. As the particle arrangement adapts to the wake structure, more particles may leave through the top boundary than added at the bottom. However, due to the use of APD, the particle arrangement is fairly uniform in the undamped region and the reduction in the number of particles is less than 0.1% of the initial number of particles. For sufficiently distant horizontal boundaries, the wall effects on the sedimentation process become negligible. As a result, the repeated shifting of the ellipse allows us to reuse the computational domain and simulate the sedimentation in an essentially infinite channel.

5.2. Validation of the boundary implementation

To ensure an accurate simulation, proper resolution, time step and domain height need to be determined. While the time step is chosen via CFL condition, appropriate resolution and domain height are found by simulating the sedimentation of an ellipse in a domain with $B = 4$. The ellipse is placed in the middle of the channel at an angle $\theta_i = 45^\circ$ while the initial particle arrangement is similar to the one given by [Tofighi et al. \(2015\)](#). The results are shown in figure 3. Since the boundaries are shifted vertically to follow the ellipse's descent,

the vertical position of the ellipse is calculated by integrating its infinitesimal movements in time. Figure 3-a plots the horizontal position of the ellipse versus its vertical position for different particle spacings of $\delta_p/a = 1/15, 1/20, 1/25$ and $1/30$ while density ratio is set to $\mathcal{D} = 1.1$. These cases are simulated in a fixed domain of height H with $H/a = 32$ where the ellipse center lies at a distance of $8a$ away from the top wall before release. The difference between vertical positions become negligible for $\delta_p/a \leq 1/25$ and ellipse orientation (not shown here) follows a similar trend. As such, we use $\delta_p/a = 1/25$ for the rest of the simulations in this study. To determine the appropriate domain height, we compare the results of three shifting boundary simulations with $H/a = 8, 16$ and 32 with the fixed domain results at $H/a = 32$. Figure 3-b plots horizontal versus vertical position for $\mathcal{D} = 1.01, 1.1$ and 1.5 . The results of shifting boundary are identical to fixed boundary for $\mathcal{D} = 1.01$ and 1.1 , even for the smallest domain size with $H/a = 8$. The trajectories for $\mathcal{D} = 1.5$ simulated in shifting boundaries converge for $H/a \geq 16$. However, there is a slight difference between trajectories of fixed and shifting boundaries in this case. This may be attributed to the boundary effects at higher Re_t in the fixed boundary configuration. We use $H/a = 16$ for the remaining simulations in this study.

Figure 4 compares the horizontal position and orientation of the ellipse computed in this study with the results of *et al.* [Xia et al. \(2009\)](#), [Suzuki and Inamuro \(2011\)](#) and [Khorasanizade and Khorasanizade and Sousa \(2016\)](#). All results are in good agreement for $\mathcal{D} = 1.1$. The position and orientation from the current simulation lie between those by [Xia et al. \(2009\)](#) and [Suzuki and Inamuro \(2011\)](#) for $\mathcal{D} = 1.01$. Our results show similar behavior to those available in the literature for $\mathcal{D} = 1.5$ and the quantitative difference falls within the acceptable range. The changes in direction (figure 4-a) are more frequent in the results of [Xia et al. \(2009\)](#) compared to those by [Suzuki and Inamuro \(2011\)](#) and [Khorasanizade and Sousa \(2016\)](#), while our results lag behind. On the other hand, when compared to the work of [Suzuki and Inamuro \(2011\)](#) and [Xia et al. \(2009\)](#), the simulations by [Khorasanizade and Sousa \(2016\)](#) predict the smallest range for horizontal displacement and change in orientation while our results exhibit

the largest range. Table 1 shows the average Reynolds number Re_t for the current simulation and literature data (Xia et al., 2009; Suzuki and Inamuro, 2011; Khorasanizade and Sousa, 2016). As it is seen, the current simulation results are in agreement with Re_t values of other numerical simulations. As such, it is possible to infer that the proposed method is able to capture the behavior of a sedimenting ellipse in an essentially infinite channel accurately.

6. Results

6.1. Blockage ratio and initial orientation

Depending on the blockage ratio, a sedimenting ellipse may have significant interactions with lateral walls of the channel. These interactions become more complicated when an external electric field is present. In their study, Xia et al. (2009) identified five different sedimentation regimes for aspect ratios of $\mathcal{B} > 9/13$. Here, we simulate the sedimentation behavior for blockage ratios of $\mathcal{B} = 1, 2$ and 4 at a density ratio of $\mathcal{D} = 1.1$. Initially, the ellipse is positioned at the center of the channel at an angle $\theta_i = 45^\circ$. We set the permittivity ratio to $\mathcal{P} = 0.05, 0.2, 0.5, 1, 2, 5$ and 20 with an Electrogravitational number of $Eg_p = 40$.

Our simulations for non-electrified cases exhibit the same behavior observed by Xia et al. (2009). During the later stages of the simulation, the ellipse follows an oscillating path for $\mathcal{B} = 1$ while it descends maintaining a horizontal orientation for $\mathcal{B} \geq 2$. The presence of an external electric field alters the sedimentation pattern by imposing a torque which tends to rotate the ellipse to align its major axis with the electric field. Table 2 shows the average Reynolds number Re_t for the cases considered here. The simulations are carried out until the ellipses descend up to 10, 20 and 40 major axis lengths for $\mathcal{B} = 1, 2$ and 4 , respectively. We observe four different patterns in the sedimenting ellipses. These are (i) vertical, (ii) oscillating, (iii) slanted and (iv) horizontal sedimentation. As evidenced by higher Re_t , wider channels result in faster sedimentation.

Following table 2, it is observed that for the narrowest channel, the fastest descent happens when no electrical field is present. The overall difference in Re_t for various \mathcal{P} is rather small for $B = 1$. However, as the channel widens, the effect of \mathcal{P} on Re_t becomes more significant. At both ends of \mathcal{P} , the ellipses sediment vertically and have the largest Re_t while the ellipse descends horizontally at $\mathcal{P} = 1$. The vertical sedimentation at $\mathcal{P} = 0.05$ and 20 persists even for $B = 8$ (not shown here). In addition to horizontal and vertical descent orientations, for $B = 4$, the ellipses show an oscillating behavior as well. The ellipses at $B = 2$ show both slanted and oscillatory motion as \mathcal{P} approaches unity.

Examining each column of table 2, we are not able to identify a clear relationship between Re_t and blockage ratio, except for vertical sedimentation cases at $\mathcal{P} = 0.05$ and 20. As B increases, the difference between consecutive Re_t values decreases. At $B = 8$, Re_t is equal to 22.76 and 22.18 for $\mathcal{P} = 0.05$ and $\mathcal{P} = 20$, respectively. It may seem that Re_t is approaching an asymptotic value in columns leading to oscillating descent, however, increasing B further to 8 leads to considerable increase in Re_t . For example, at $\mathcal{P} = 5$ and $B = 8$, Re_t is equal to 17.01. It is possible for a clear trend to emerge at higher blockage ratios for non-vertical sedimentation, however, we have not investigated this matter any further in this work.

Figure 5 shows position, orientation and ellipse profiles for $\mathcal{P} = 0.05, 0.2, 0.5, 1, 2$ and 20 for $B = 2$. The ellipse paths, plotted in figure 5-a, converge to the channel center for $\mathcal{P} = 0.05, 1$ and 20 at the early stages of the simulation and later for $\mathcal{P} = 0.5$ (not shown here). In contrast, $\mathcal{P} = 0.2$ and 2 show a very low amplitude oscillation over a path to the left of centerline. The orientation of the sedimenting ellipse is highly dependent on the permittivity ratio (figure 5-b). The ellipse sediments vertically for $\mathcal{P} = 0.05$ and 20 while it descends horizontally when $\mathcal{P} = 1$ and 0.5. Setting $\mathcal{P} = 0.2$ results in a slanted sedimentation at an average angle of 77.2° at $x = -0.133$ while at $\mathcal{P} = 2$, the ellipse descends at $\theta = 22.8^\circ$ and $x = -0.178$. [Xia et al. \(2009\)](#) have also observed such slanted descent in non-electrified cases and identified a strong dependence in sedimentation behavior with respect to the initial angle. We

repeated the simulation at $\mathcal{P} = 0.2$ for $\theta_i = 15^\circ, 30^\circ, 60^\circ$ and 75° to investigate this effect. However, we found negligible difference in sedimentation angle and position compared to $\theta_i = 45^\circ$. The profiles of the ellipses shown in figure 5-c provide a clearer picture of the ellipse behavior during the sedimentation.

To assess the effects of initial orientation on the ellipse behavior, we simulated the sedimentation for a density ratio of $\mathcal{D} = 1.1$ for $\mathcal{P} = 20, 5$ and 0.05 at $Eg_p = 40$. The ellipse is released from channel center. Two blockage ratios of $\mathcal{B} = 4$ and 8 are investigated and initial angles are set to $\theta_i = 15^\circ, 30^\circ, 45^\circ, 60^\circ$ and 75° . The cases with $\mathcal{P} = 20$ and 0.05 become vertical soon after release, regardless of their initial orientation. As for $\mathcal{P} = 5$, all initial orientations result in the same oscillating pattern, however, the vertical distance traveled to reach the periodic angular motion is different in each case. Table 3 shows the distance traveled until a periodic angular oscillation is obtained. As expected, the ellipse reaches periodic oscillation at a further distance when released at larger initial angles. There is a significant jump in traveled distance for $\theta_i \geq 45^\circ$ at $\mathcal{B} = 4$ which is not as significant for $\mathcal{B} = 8$. For the narrower channel, the ellipse released at $\theta \geq 45^\circ$ approaches the vertical wall and descends briefly alongside it before returning to the channel center. While close to the wall, the oscillatory motion is suppressed and the amplitude starts to increase only after the ellipse returned to the middle of the channel. Since the ellipse-wall interaction in the wider channel is not as significant as the narrower channel, the jump in required distance is less pronounced for $\mathcal{B} = 8$.

6.2. The effect of electric field intensity

Changing field intensity provides a direct method to influence the ellipse behavior and the sedimentation trajectory depends on the interplay of hydrodynamic and electrical forces. To observe these effects, we simulate the sedimentation behavior for three density ratios of $\mathcal{D} = 1.01, 1.1$ and 1.5 for $\mathcal{B} = 4$. The ellipse is released from channel center at an initial angle of $\theta_i = 45^\circ$. Without an external electric field, the ellipse sediments in a horizontal orientation for $\mathcal{D} = 1.01$ and 1.1 while it shows an oscillatory behavior at $\mathcal{D} = 1.5$. Permit-

tivity ratios for electrified cases are similar to those of previous section while $Eg_p = 40, 10$ and 5 . According to the definition of Eg_p (*cf.* equation (2)), a larger electric intensity results in a smaller Eg_p .

6.2.1. Average quantities

Table 4 shows average Reynolds number Re_t for the cases studied here. All cases with $\mathcal{D} = 1.01$ descend vertically for $\mathcal{P} \neq 1$ and have similar Re_t . This means that electric torque is dominant and rotates the major axis to align with the electric field. As the behavior is similar for lower Eg_p , we do not tabulate the results here. An increase in density ratio to $\mathcal{D} = 1.1$ leads to comparable hydrodynamic and electrical torques. For $Eg_p = 40$, the range of sedimentation patterns was discussed in the previous section. An increase in the field intensity results in a shift from oscillating to vertical sedimentation pattern for $\mathcal{P} = 0.2$ and 5 while it induces a shift from horizontal descent to oscillatory motion for $\mathcal{P} = 0.5$ and 2 . It is worth mentioning that Re_t have similar values for all vertical sedimentations. A further decrease in Eg_p results in vertical sedimentation for $\mathcal{P} \neq 1$ at $\mathcal{D} = 1.1$ and is not shown here. Since the non-electrified sedimentation pattern at $\mathcal{D} = 1.5$ is oscillatory itself, the sedimentation patterns of electrified cases remain oscillatory for a wider range of Eg_p . A general observation is that Re_t increases slightly further away from $\mathcal{P} = 1$ for oscillatory motion and a significant increase occurs when the ellipse descends vertically.

To further investigate the range of oscillatory motions observed in $\mathcal{D} = 1.5$, figure 6 plots average Reynolds Re_t , oscillation frequency ωt_c , oscillation amplitude Δx and angular sweep $\Delta\theta/\pi$ for all cases with oscillatory sedimentation pattern. As mentioned before, Re_t increases as \mathcal{P} goes further away from unity. As the electrical torque counters the hydrodynamics torque on the ellipse, the oscillation frequency is reduced for lower Eg_p as well (figure 6-b). Figure 6-c shows that larger Eg_p and $|1 - \mathcal{P}|$ result in higher oscillation amplitude. A similar trend is observed for the angular sweep in figure 6-d. An increase in channel width to $\mathcal{B} = 8$ results in similar trends (no shown here). In comparison to $\mathcal{B} = 4$, the ellipse sedimenting in a channel with $\mathcal{B} = 8$ shows reduced

oscillation frequency, amplitude and swept angle while it has larger Re_t .

6.2.2. Transient behavior

Figure 7 shows sedimentation path and ellipse profile for $y = 0$ to 20 as well as a closeup of streamlines at $y = 20$ for $\mathcal{D} = 1.5$ and $\mathcal{P} = 0.2$. As it is seen in figure 7-a, for lower Eg_p , the angle between the major axis of ellipse and the tangent line to sedimentation path remains small for larger portions of the trajectory. While the major axis of the ellipse is mostly perpendicular to its trajectory for $Eg_p = 40$, the angle between major axis and sedimentation path remains small for large portions of the descent at $Eg_p = 5$. This results in the wider path and larger oscillation amplitude observed. Furthermore, as the ellipse rotates between two highly slanted orientations, a larger angular oscillation amplitude is observed for $Eg_p = 5$. The effects of sedimentation trajectory on vortical structures in the vicinity of the ellipse is shown in figure 7-b where the vortices are further stretched at smaller Eg_p .

To further investigate the effects of electric field on the sedimentation pattern, the electric ($\mathbf{T}_{(e)}$), hydrodynamic ($\mathbf{T}_{(h)}$) and total ($\mathbf{T}_{(t)}$) torques applied to the ellipse as well as position and orientation of the ellipse are shown in figure 8. The torques per unit depth are made dimensionless using $\rho_f g_\infty a A$ where A denotes the ellipse area. To calculate the electric torque, the moment due to the force applied to each particle through equation (10) is summed over the ellipse particles. The hydrodynamic torque is calculated in a similar fashion while the total torque is the summation of electric and hydrodynamic parts. Each column in figure 8 plots two oscillation cycles for $Eg_p = 40, 10$ and 5 , corresponding to cases shown in figure 7. In all cases, the electric torque counteracts the dominant hydrodynamic term. While the overall magnitude of the total torque remains comparable, the profiles differ significantly, especially at $Eg_p = 5$. This may be traced to the electric torque applied to the ellipse. It is known that the maximum electric torque happens at $\theta = 45^\circ$ (House et al., 2012). For $Eg_p = 40$, the magnitude of electric torque is sufficient to rotate the ellipse beyond $\theta = 45^\circ$, however, it is not enough to reach a vertical orientation. As θ increases beyond

the 45° mark, the electric torque is reduced and the hydrodynamic term rotates the ellipse back toward $\theta = 45^\circ$. This momentarily increases the electric torque opposing the rotation as θ decreases, passing the 45° mark. The overall effect is the longer slanted sedimentation periods observed in figure 7-a, contributing to a faster descent (figure 6-a).

7. Conclusions

An incompressible smoothed particle hydrodynamics method for two dimensional simulation of unlimited sedimentation of rigid bodies in Newtonian fluids is presented. The scheme uses viscous penalty and rigidity constraints to impose the rigid behavior. The unlimited descent or ascent is achieved by periodic shifting of computational domain to center on the feature of interest. Modified boundary conditions are introduced to add or discard particles after each shift in the computational domain. The method is tested for sedimentation of a single elliptic disc and the results are in quantitative agreement with literature data. This shows that the proposed method is capable of simulating unlimited descent or ascent of features of interest (bubbles, drops or rigid bodies) using smoothed particle hydrodynamics method.

The proposed method is further used to simulate the sedimentation of a single elliptic disc in an external electric field. Our results show that it is possible to increase the ellipse sedimentation velocity for wider channels by applying the electric field. While the sedimentation path at the early stages was highly affected by the initial orientation, we observed no particular difference between sedimentation pattern at the later stages of simulation. Introduction of the electric field at larger density ratios, where a non-electrified ellipse sediments in an oscillatory pattern, reduces the oscillation frequency while sedimentation velocity, oscillation amplitude and swept angle are increased.

Acknowledgments

NT acknowledges financial support from Mitacs-Accelerate program under the grant number IT08354. MY gratefully acknowledge financial support provided by the Scientific and Technological Research Council of Turkey (TUBITAK) for grant number 112M721. AS gratefully acknowledges the financial support provided by the Natural Sciences and Engineering Research Council (NSERC) for the Canada Research Chair in Computational and Experimental Mechanics. JJF acknowledges support by the NSERC Discovery grant No. 05862. Computational resources were supported in part by WestGrid (www.westgrid.ca) and Compute Canada Calcul Canada (www.computecanada.ca).

References

- Adami, S., Hu, X.Y., Adams, N.A., 2012. A generalized wall boundary condition for smoothed particle hydrodynamics. *J. Comput. Phys.* 231, 7057–7075. doi:[10.1016/j.jcp.2012.05.005](https://doi.org/10.1016/j.jcp.2012.05.005).
- Ai, Y., Qian, S., 2010. DC dielectrophoretic particle-particle interactions and their relative motions. *J. Colloid Interface Sci.* 346, 448–454. doi:[10.1016/j.jcis.2010.03.003](https://doi.org/10.1016/j.jcis.2010.03.003).
- Aidun, C.K., Lu, Y.N., Ding, E.J., 1998. Direct analysis of particulate suspensions with inertia using the discrete Boltzmann equation. *J. Fluid Mech.* 373, 287–311. doi:[10.1017/S0022112098002493](https://doi.org/10.1017/S0022112098002493).
- Bonnecaze, R.T., Brady, J.F., 1992. Dynamic simulation of an electrorheological fluid. *J. Chem. Phys.* 96, 2183–2202. doi:[10.1063/1.462070](https://doi.org/10.1063/1.462070).
- Chang, Y.J., Keh, H.J., 2013. Sedimentation of a charged porous particle in a charged cavity. *J. Phys. Chem. B* 117, 12319–12327. doi:[10.1021/jp407805x](https://doi.org/10.1021/jp407805x).
- Cox, R.G., 1965. The steady motion of a particle of arbitrary shape at small Reynolds numbers. *J. Fluid Mech.* 23, 625–643. doi:[10.1017/S0022112065001593](https://doi.org/10.1017/S0022112065001593).

- Ern, P., Risso, F., Fabre, D., Magnaudet, J., 2012. Wake-induced oscillatory paths of bodies freely rising or falling in fluids. *Annu. Rev. Fluid Mech.* 44, 97–121. doi:[10.1146/annurev-fluid-120710-101250](https://doi.org/10.1146/annurev-fluid-120710-101250).
- Federico, I., Marrone, S., Colagrossi, A., Aristodemo, F., Antuono, M., 2012. Simulating 2D open-channel flows through an SPH model. *Eur. J. Mech. B-Fluids* 34, 35–46. doi:[10.1016/j.euromechflu.2012.02.002](https://doi.org/10.1016/j.euromechflu.2012.02.002).
- Feng, J., Hu, H.H., Joseph, D.D., 1994. Direct simulation of initial-value problems for the motion of solid bodies in a Newtonian fluid .1. Sedimentation. *J. Fluid Mech.* 261, 95–134. doi:[10.1017/S0022112094000285](https://doi.org/10.1017/S0022112094000285).
- Feng, J., Joseph, D.D., 1995. The unsteady motion of solid bodies in creeping flows. *J. Fluid Mech.* 303, 83–102. doi:[10.1017/S0022112095004186](https://doi.org/10.1017/S0022112095004186).
- Ferrand, M., Laurence, D.R., Rogers, B.D., Violeau, D., Kassiotis, C., 2013. Unified semi-analytical wall boundary conditions for inviscid, laminar or turbulent flows in the meshless SPH method. *Int. J. Numer. Methods Fluids* 71, 446–472. doi:[10.1002/fld.3666](https://doi.org/10.1002/fld.3666).
- Field, S.B., Klaus, M., Moore, M.G., Nori, F., 1997. Chaotic dynamics of falling disks. *Nature* 388, 252–254. doi:[10.1038/40817](https://doi.org/10.1038/40817).
- Gingold, R.A., Monaghan, J.J., 1977. Smoothed particle hydrodynamics: theory and application to non-spherical stars. *Mon. Not. R. Astron. Soc.* 181, 375–389. doi:[10.1093/mnras/181.3.375](https://doi.org/10.1093/mnras/181.3.375).
- He, Y., Bayly, A.E., Hassanpour, A., Muller, F., Wu, K., Yang, D., 2018. A GPU-based coupled SPH-DEM method for particle-fluid flow with free surfaces. *Powder Technol.* 338, 548–562. doi:[10.1016/j.powtec.2018.07.043](https://doi.org/10.1016/j.powtec.2018.07.043).
- Hirschler, M., Kunz, P., Huber, M., Hahn, F., Nieken, U., 2016. Open boundary conditions for ISPH and their application to micro-flow. *J. Comput. Phys.* 307, 614–633. doi:[10.1016/j.jcp.2015.12.024](https://doi.org/10.1016/j.jcp.2015.12.024).

- Hosseini, S.M., Feng, J.J., 2011. Pressure boundary conditions for computing incompressible flows with SPH. *J. Comput. Phys.* 230, 7473–7487. doi:[10.1016/j.jcp.2011.06.013](https://doi.org/10.1016/j.jcp.2011.06.013).
- House, D.L., Luo, H., Chang, S., 2012. Numerical study on dielectrophoretic chaining of two ellipsoidal particles. *J. Colloid Interface Sci.* 374, 141–149. doi:[10.1016/j.jcis.2012.01.039](https://doi.org/10.1016/j.jcis.2012.01.039).
- Joubert, J.C., Wilke, D.N., Govender, N., Pizette, P., Tuzun, U., Abriak, N.E., 2020. 3D gradient corrected SPH for fully resolved particle-fluid interactions. *Appl. Math. Model.* 78, 816–840. doi:[10.1016/j.apm.2019.09.030](https://doi.org/10.1016/j.apm.2019.09.030).
- Khorasanizade, S., Sousa, J.M.M., 2016. A two-dimensional Segmented Boundary Algorithm for complex moving solid boundaries in Smoothed Particle Hydrodynamics. *Comput. Phys. Commun.* 200, 66–75. doi:[10.1016/j.cpc.2015.10.025](https://doi.org/10.1016/j.cpc.2015.10.025).
- Lastiwka, M., Basa, M., Quinlan, N.J., 2009. Permeable and non-reflecting boundary conditions in SPH. *Int. J. Numer. Methods Fluids* 61, 709–724. doi:[10.1002/fld.1971](https://doi.org/10.1002/fld.1971).
- Lee, E., Yen, C.B., Hsu, J.P., 2000. Sedimentation of a nonconducting sphere in a spherical cavity. *J. Phys. Chem. B* 104, 6815–6820. doi:[10.1021/jp993716s](https://doi.org/10.1021/jp993716s).
- Lucy, L.B., 1977. A numerical approach to the testing of the fission hypothesis. *Astron. J.* 82, 1013–1024. doi:[10.1086/112164](https://doi.org/10.1086/112164).
- Monaghan, J.J., 2012. Smoothed particle hydrodynamics and its diverse applications. *Annu. Rev. Fluid Mech.* 44, 323–346. doi:[10.1146/annurev-fluid-120710-101220](https://doi.org/10.1146/annurev-fluid-120710-101220).
- Monaghan, J.J., Kajtar, J.B., 2009. SPH particle boundary forces for arbitrary boundaries. *Comput. Phys. Commun.* 180, 1811–1820. doi:[10.1016/j.cpc.2009.05.008](https://doi.org/10.1016/j.cpc.2009.05.008).

- Monaghan, J.J., Kocharyan, A., 1995. SPH simulation of multiphase flow. *Comput. Phys. Commun.* 87, 225–235. doi:[10.1016/0010-4655\(94\)00174-Z](https://doi.org/10.1016/0010-4655(94)00174-Z).
- Morris, J.P., 1996. A study of the stability properties of smooth particle hydrodynamics. *Publ. Astron. Soc. Aust.* 13, 97–102. URL: <http://adsabs.harvard.edu/abs/1996PASA...13...97M>.
- Morris, J.P., Fox, P.J., Zhu, Y., 1997. Modeling low Reynolds number incompressible flows using SPH. *J. Comput. Phys.* 136, 214–226. doi:[10.1006/jcph.1997.5776](https://doi.org/10.1006/jcph.1997.5776).
- Newman, H.D., Yethiraj, A., 2015. Clusters in sedimentation equilibrium for an experimental hard-sphere-plus-dipolar Brownian colloidal system. *Sci. Rep.* 5, 13572. doi:[10.1038/srep13572](https://doi.org/10.1038/srep13572).
- Parthasarathy, M., Klingenber, D.J., 1996. Electrorheology: mechanisms and models. *Mater. Sci. Eng. R-Rep.* 17, 57–103. doi:[10.1016/0927-796X\(96\)00191-X](https://doi.org/10.1016/0927-796X(96)00191-X).
- Robinson, M., Ramaioli, M., Luding, S., 2014. Fluid-particle flow simulations using two-way-coupled mesoscale SPH-DEM and validation. *Int. J. Multiph. Flow* 59, 121–134. doi:[10.1016/j.ijmultiphaseflow.2013.11.003](https://doi.org/10.1016/j.ijmultiphaseflow.2013.11.003).
- Saville, D.A., 1997. Electrohydrodynamics: The Taylor-Melcher leaky dielectric model. *Annu. Rev. Fluid Mech.* 29, 27–64. doi:[10.1146/annurev.fluid.29.1.27](https://doi.org/10.1146/annurev.fluid.29.1.27).
- Shao, S.D., Lo, E.Y.M., 2003. Incompressible SPH method for simulating Newtonian and non-Newtonian flows with a free surface. *Adv. Water Resour.* 26, 787–800. doi:[10.1016/S0309-1708\(03\)00030-7](https://doi.org/10.1016/S0309-1708(03)00030-7).
- Sullivan, M., Zhao, K., Harrison, C., Austin, R., Megens, M., Hollingsworth, A., Russel, W., Cheng, Z., Mason, T., Chaikin, P., 2003. Control of colloids with gravity, temperature gradients, and electric fields. *J. Phys.-Condes. Matter* 15, 11–18. doi:[10.1088/0953-8984/15/1/302](https://doi.org/10.1088/0953-8984/15/1/302).

- Suzuki, K., Inamuro, T., 2011. Effect of internal mass in the simulation of a moving body by the immersed boundary method. *Comput. Fluids* 49, 173–187. doi:[10.1016/j.compfluid.2011.05.011](https://doi.org/10.1016/j.compfluid.2011.05.011).
- Swaminathan, T.N., Mukundakrishnan, K., Hu, H.H., 2006. Sedimentation of an ellipsoid inside an infinitely long tube at low and intermediate Reynolds numbers. *J. Fluid Mech.* 551, 357–385. doi:[10.1017/S0022112005008402](https://doi.org/10.1017/S0022112005008402).
- Tofighi, N., Ozbulut, M., Rahmat, A., Feng, J.J., Yildiz, M., 2015. An incompressible smoothed particle hydrodynamics method for the motion of rigid bodies in fluids. *J. Comput. Phys.* 297, 207–220. doi:[10.1016/j.jcp.2015.05.015](https://doi.org/10.1016/j.jcp.2015.05.015).
- Tofighi, N., Ozbulut, M., Suleman, A., Feng, J.J., Yildiz, M., 2019. Dielectrophoretic interaction of circular particles in a uniform electric field. *Eur. J. Mech. B/Fluids* 78, 194–202. doi:[10.1016/j.euromechflu.2019.07.002](https://doi.org/10.1016/j.euromechflu.2019.07.002).
- Velev, O.D., Gangwal, S., Petsev, D.N., 2009. Particle-localized AC and DC manipulation and electrokinetics. *Annu. Rep. Prog. Chem., Sect. C: Phys. Chem.* 105, 213–246. doi:[10.1039/B803015B](https://doi.org/10.1039/B803015B).
- Xia, Z., Connington, K.W., Rapaka, S., Yue, P., Feng, J.J., Chen, S., 2009. Flow patterns in the sedimentation of an elliptical particle. *J. Fluid Mech.* 625, 249–272. doi:[10.1017/S0022112008005521](https://doi.org/10.1017/S0022112008005521).
- Yang, X., Huang, H., Lu, X., 2015. Sedimentation of an oblate ellipsoid in narrow tubes. *Phys. Rev. E* 92, 063009. doi:[10.1103/PhysRevE.92.063009](https://doi.org/10.1103/PhysRevE.92.063009).
- Yildiz, M., Rook, R.A., Suleman, A., 2009. SPH with the multiple boundary tangent method. *Int. J. Numer. Methods Eng.* 77, 1416–1438. doi:[10.1002/nme.2458](https://doi.org/10.1002/nme.2458).
- Zainali, A., Tofighi, N., Shadloo, M.S., Yildiz, M., 2013. Numerical investigation of Newtonian and non-Newtonian multiphase flows using ISPH method. *Comput. Meth. Appl. Mech. Eng.* 254, 99–113. doi:[10.1016/j.cma.2012.10.005](https://doi.org/10.1016/j.cma.2012.10.005).

Zhang, Z.L., Walayat, K., Chang, J.Z., Liu, M.B., 2018. Meshfree modeling of a fluid-particle two-phase flow with an improved SPH method. *Int. J. Numer. Methods Fluids* 116, 530–569. doi:[10.1002/nme.5935](https://doi.org/10.1002/nme.5935).

Zhang, Z.L., Walayat, K., Huang, C., Chang, J.Z., Liu, M.B., 2019. A finite particle method with particle shifting technique for modeling particulate flows with thermal convection. *Int. J. Heat Mass Transf.* 128, 1245–1262. doi:[10.1016/j.ijheatmasstransfer.2018.09.074](https://doi.org/10.1016/j.ijheatmasstransfer.2018.09.074).

Table 1: Comparison of average Reynolds number Re_t for non-electrified ellipse sedimentation at $\mathcal{B} = 4$ and $\theta_i = 45^\circ$.

\mathcal{D}	1.01	1.1	1.5
Current Simulation	2.15	13.5	33.8
Xia et al. (2009)	2.08	12.9	33.4
Suzuki and Inamuro (2011)	1.92	12.6	32.9
Khorasanizade and Sousa (2016)	—	14.6	36.1

Table 2: Average Reynolds Re_t for different blockage ratios at $\mathcal{D} = 1.1$, $\text{Eg}_p = 40$ and $\theta_i = 45^\circ$. Data in table cells indicate that the ellipse is in (roman) vertical descent, (italic) oscillating descent, (italic underline) slanted descent or (roman underline) horizontal descent.

\mathcal{P}	0.05	0.2	0.5	1	2	5	20
$\mathcal{B} = 1$	1.98	2.05	2.25	2.51	<i>2.16</i>	2.11	2.24
$\mathcal{B} = 2$	12.17	<u>11.61</u>	<u>5.40</u>	<u>5.13</u>	<u>6.33</u>	11.97	11.88
$\mathcal{B} = 4$	19.88	<i>13.68</i>	<u>13.55</u>	<u>13.50</u>	<u>13.46</u>	<u>13.43</u>	19.44

Table 3: Vertical distance required to achieve a periodic oscillation for sedimenting ellipses released from different initial orientations at $\mathcal{D} = 1.1$, $\mathcal{P} = 5$ and $\text{Eg}_p = 40$.

θ_i	15°	30°	45°	60°	75°
$\mathcal{B} = 4$	34	34.7	146.9	160.3	166.4
$\mathcal{B} = 8$	27.6	29.4	40.7	44.8	49.9

Table 4: Average Reynolds Re_t for different field intensities for $\mathcal{B} = 4$ and $\theta_i = 45^\circ$. Data in table cells indicate that the ellipse is in (roman) vertical descent, (italic) oscillating descent or (roman underline) horizontal descent.

\mathcal{P}	0.05	0.2	0.5	1	2	5	20
$\mathcal{D} = 1.01$, $\text{Eg}_p = 40$	3.13	3.15	3.10	<u>2.22</u>	3.04	2.97	3.03
$\mathcal{D} = 1.1$, $\text{Eg}_p = 40$	19.88	<i>13.68</i>	<u>13.55</u>	<u>13.50</u>	<u>13.46</u>	<u>13.43</u>	19.44
$\mathcal{D} = 1.1$, $\text{Eg}_p = 10$	20.07	20.01	<i>13.7</i>	<u>13.50</u>	<u>13.43</u>	19.92	19.85
$\mathcal{D} = 1.5$, $\text{Eg}_p = 40$	<i>34.68</i>	<i>34.03</i>	<i>33.81</i>	<i>33.75</i>	<i>33.76</i>	<i>33.91</i>	<i>36.42</i>
$\mathcal{D} = 1.5$, $\text{Eg}_p = 10$	<i>40.02</i>	<i>35.64</i>	<i>33.94</i>	<i>33.75</i>	<i>33.88</i>	<i>37.26</i>	56.14
$\mathcal{D} = 1.5$, $\text{Eg}_p = 5$	56.52	<i>39.56</i>	<i>34.16</i>	<i>33.75</i>	<i>34.58</i>	56.99	56.71

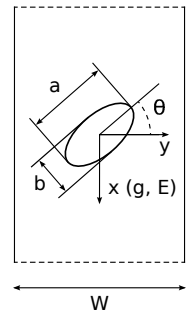


Figure 1: Schematic of a sedimenting elliptic disc

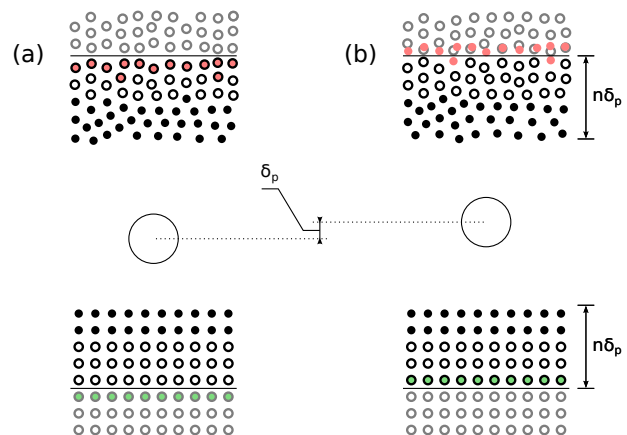


Figure 2: Schematic of the shifting boundary condition.

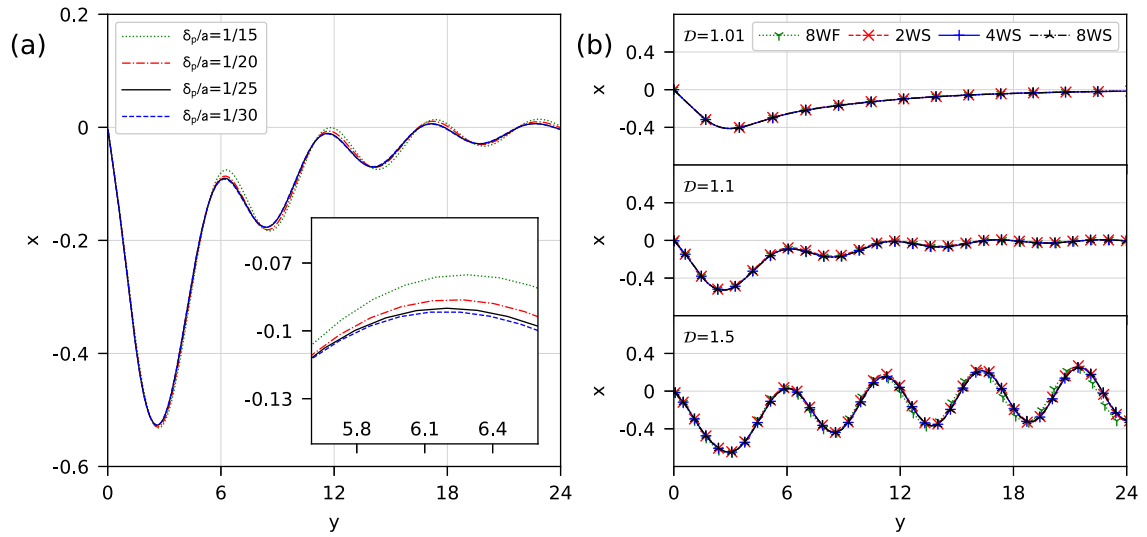


Figure 3: Horizontal position of the ellipse versus its vertical position for $B = 4$ and $\theta_i = 45^\circ$; (a) for different particle spacings at $D = 1.1$; (b) for different density ratios at $H/a = 32$ and fixed boundary (8WF), $H/a = 8$ and shifting boundary (2WS), $H/a = 16$ and shifting boundary (4WS) and $H/a = 32$ and shifting boundary (8WS).

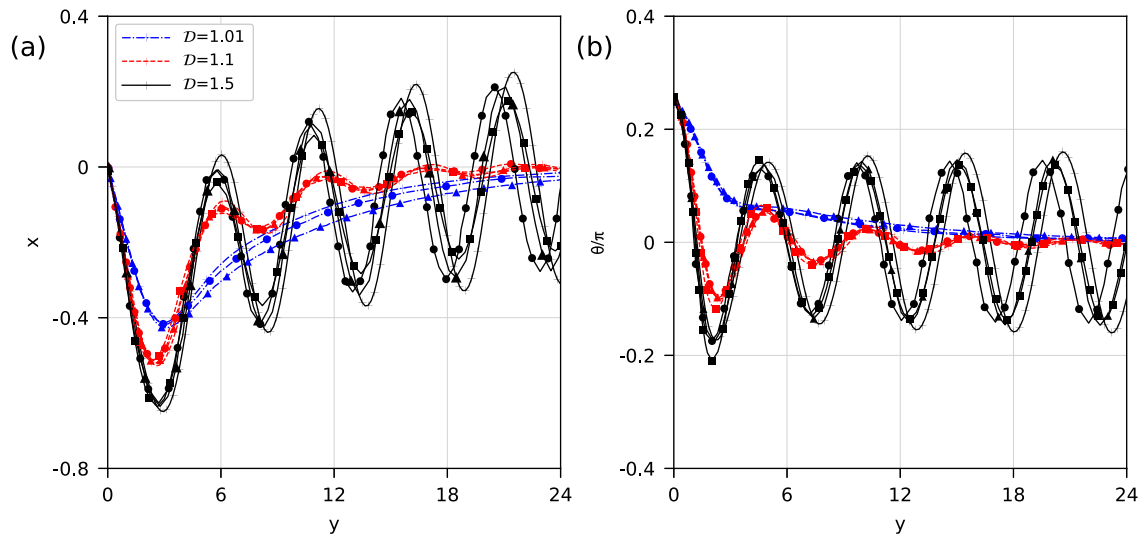


Figure 4: Horizontal position (a) and orientation of the ellipse (b) versus its vertical position at different density ratios for $\mathcal{B} = 4$ and $\theta_i = 45^\circ$; (lines) current simulation, (circles) Xia et al. (2009), (triangles) Suzuki and Inamuro (2011), (squares) Khorasanizade and Sousa (2016).

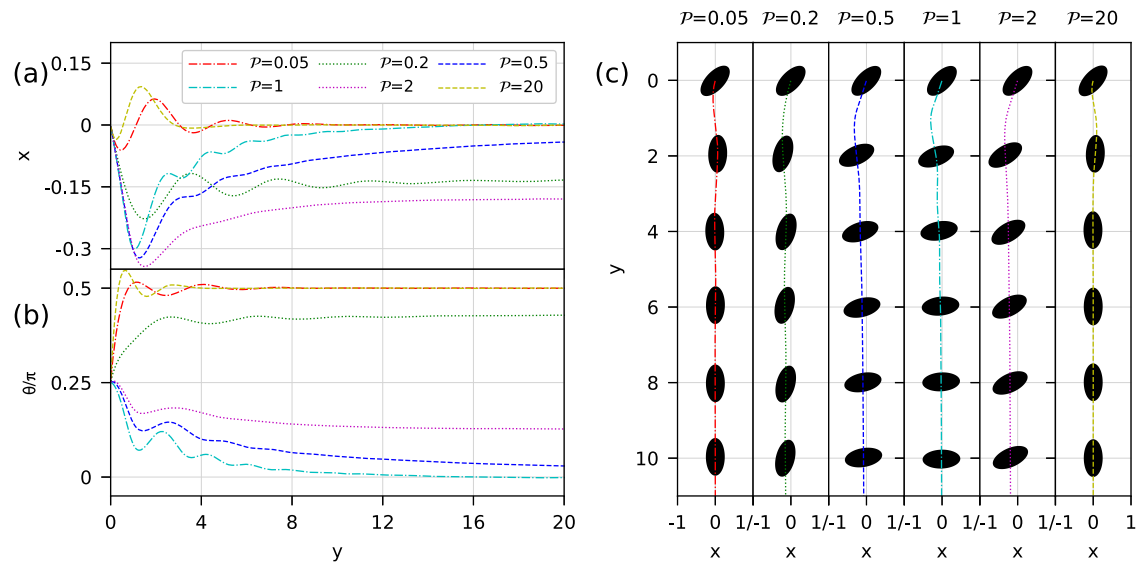


Figure 5: Sedimentation for $D = 1.1$, $B = 2$ and $Eg_p = 40$; Horizontal position (a) and orientation of the ellipse (b) versus vertical position at different permittivity ratios; (c) Sedimentation trajectory and ellipse profile for different permittivity ratios.

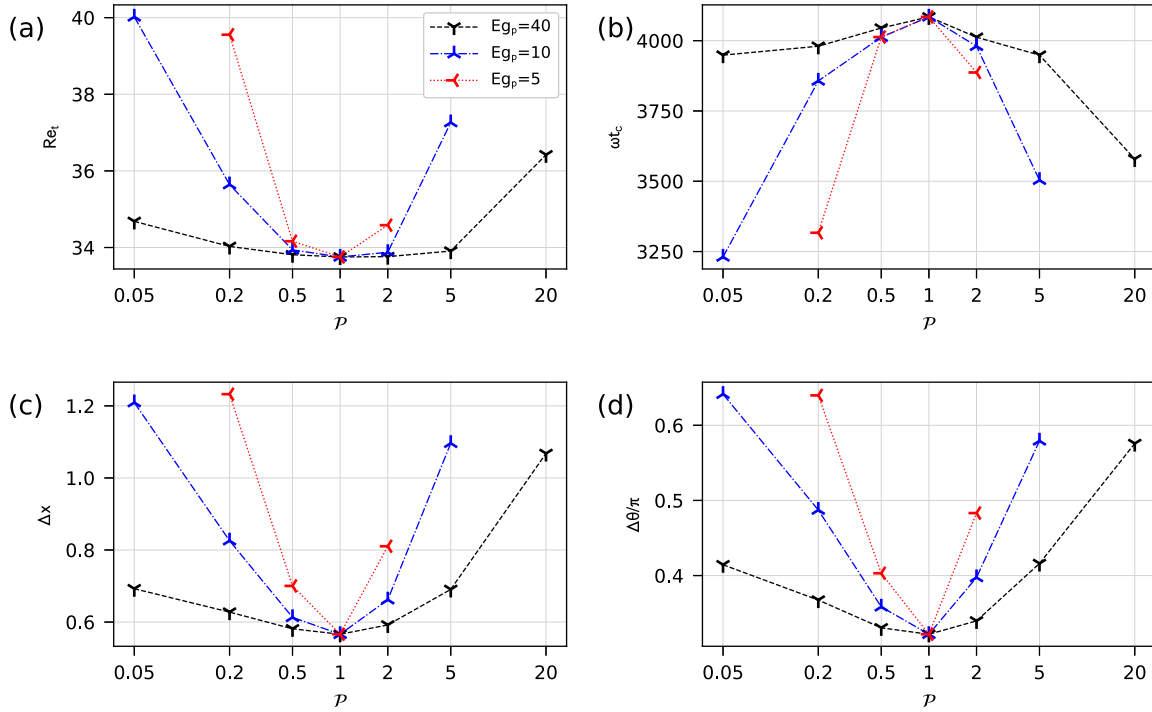


Figure 6: Effect of change in Eg_p and \mathcal{P} on average Reynolds number Re_t (a), oscillation frequency ωt_c (b), oscillation amplitude Δx (c) and swept angle $\Delta\theta/\pi$ (d). The data belong to the cases in table 4 where the ellipse is sedimenting in an oscillatory pattern at $\mathcal{D} = 1.5$, $\mathcal{B} = 4$ and $\theta_i = 45^\circ$.

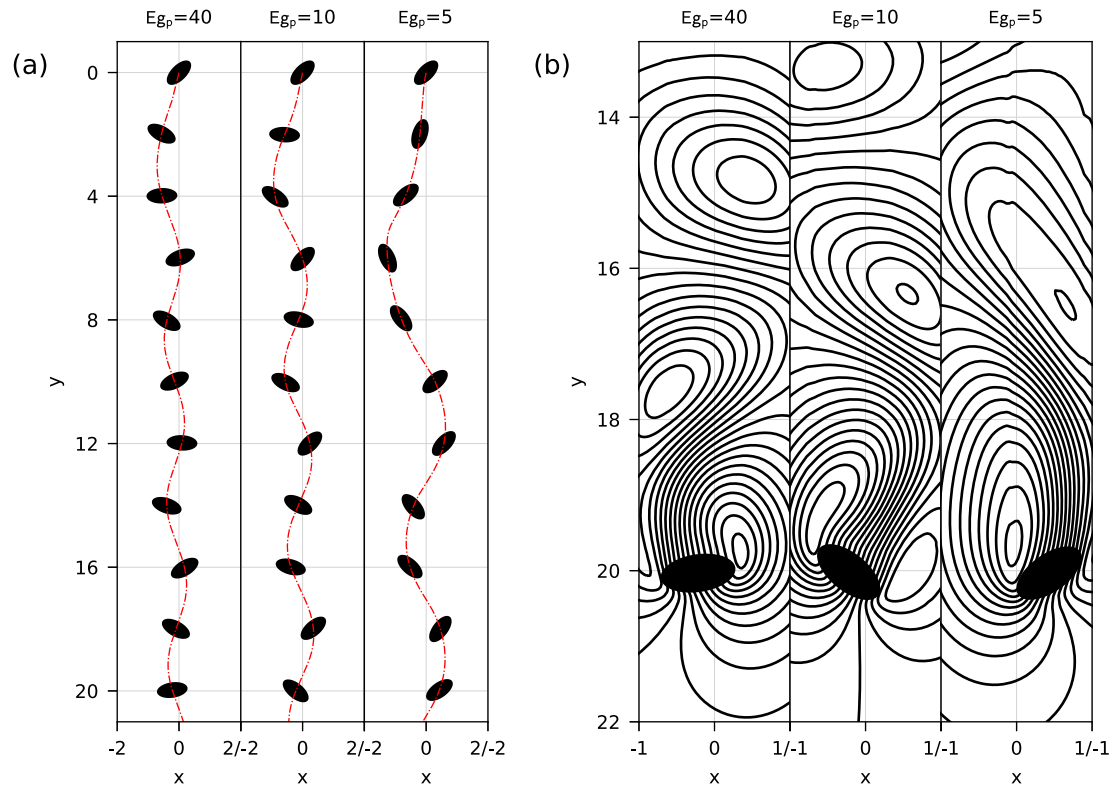


Figure 7: Ellipse sedimentation at $D = 1.5$, $B = 4$, $P = 0.2$ and $\theta_i = 45^\circ$; (a) sedimentation trajectory and ellipse profile for different Eg_p ; (b) closeup of the ellipse profile and streamlines at $y = 20$ for different Eg_p .

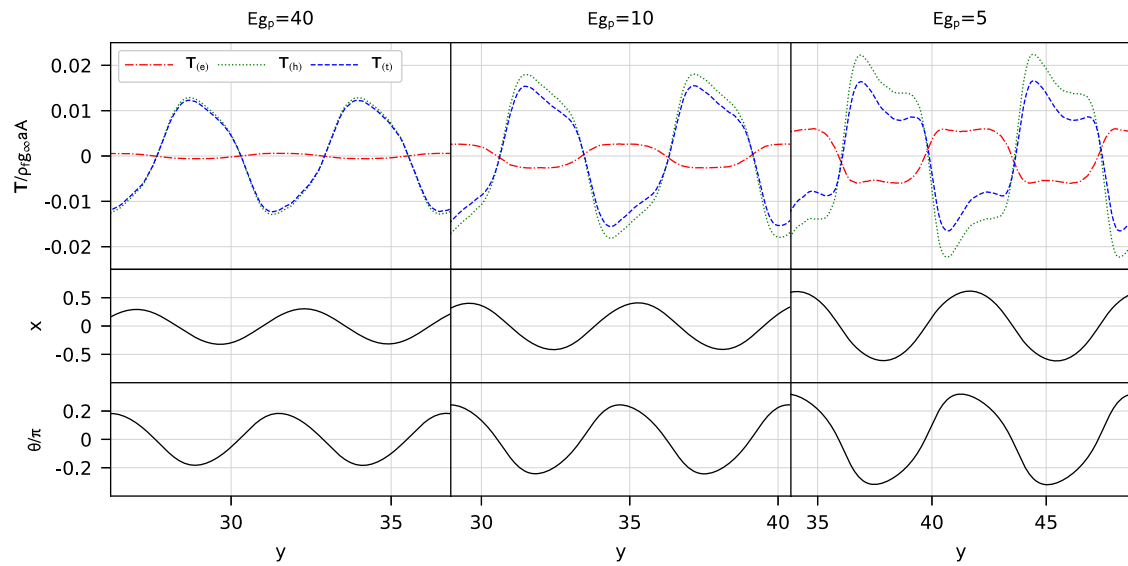


Figure 8: Electric ($\mathbf{T}_{(e)}$), hydrodynamic ($\mathbf{T}_{(h)}$) and total ($\mathbf{T}_{(t)}$) torques applied to the ellipse versus vertical position for different field intensities for $\mathcal{D} = 1.5$, $\mathcal{B} = 4$, $\mathcal{P} = 0.2$ and $\theta_i = 45^\circ$. Horizontal position and orientation of the ellipse are plotted in lower rows.